Research Article

Photodegradation of Methylene Blue Using Carbon-Doped ZnSn(OH)$_6$ Composite Coated on Membrane

Ernso Fenelon [iD],[1] **Achmad Chusnun Ni'am,**[2] **Truc-Mai Thi Nguyen,**[3] **Ying-Fu Lin,**[4] **Ya-Fen Wang,**[4,5] **and Sheng-Jie You** [iD][4,5]

[1]*Centre de Recherche Interdisciplinaire Pour la Vulgarisation Agricole et le Développement Local (CREIVADEL), Université Notre Dame d'Haïti, Faculté d'Agronomie, BP HT 8110, Redon, Torbeck, Haiti*
[2]*Department of Environmental Engineering, Institut Teknologi Adhi Tama Surabaya, Arief Rachman Hakim Road No. 100, Surabaya 60117, Indonesia*
[3]*Center for Environmental Toxin and Emerging-Contaminant Research, Cheng Shiu University, Kaohsiung 83347, Taiwan*
[4]*Department of Environmental Engineering, Chung Yuan Christian University, Taoyuan 320, Taiwan*
[5]*Center for Environmental Risk Management, Chung Yuan Christian University, 200 Chung Pei Road, Chungli 320, Taiwan*

Correspondence should be addressed to Ernso Fenelon; efenelon62@gmail.com and Sheng-Jie You; sjyou@cycu.edu.tw

The dye contamination of water is a global concern in the environment. In this study, the photocatalytic technology and membrane module were combined to improve the surface distribution of the active species of the catalyst for better degradation of the methylene blue (MB) dye under visible light. ZnSn(OH)$_6$ was chosen due to carbon's complex metal oxide doped to facilitate the application under visible light. The numerous characterizations were analyzed in the composites to verify the consistency of the optimum degradation of MB over the catalyst coated on the membrane. During the preparation of the ZnSn(OH)$_6$ composite, the results confirmed that different reaction times and amounts of sodium hydroxide significantly affected the pollutant's degradation. The carbon-doped composite denoted the largest surface area and increased the catalyst's reactive sites on the membrane. The photocatalytic activity test showed that 1% carbon doped on ZnSn(OH)$_6$ prepared at 160°C by hydrothermal method coated on the membrane had the optimal degradation of 89.74% of MB. This study contributes to the ongoing study and development of photocatalytic membranes for the photodegradation of wastewater treatment.

1. Introduction

Wastewater contamination is becoming an environmental and industrial challenge [1]. In case, dye elimination is one of the most difficult challenges for textile manufacturing operations [2]. In addition, synthetic dyes in the environment present a challenge for wastewater treatment [3]. The degradation of dyes from wastewater is essential owing to their effects on water quality in the environment, even in low quantities [4]. Due to the potential risk of dye wastewater in the environment, effective treatment should be applied before discharging [5].

Various technologies and procedures for environmental remediation have been established in recent decades for dye removal, including adsorption and photocatalysis [6]. The photocatalytic method proved the efficient result in reducing the synthetic dyes in wastewater due to its simple application in the degradation of dyes processes [7] because photocatalyst applies light energy with the potential level to provide energy for the chemical reaction [8–10]. The catalyst, Zinc-tin bimetal hydroxide, and oxide (ZnSn(OH)$_6$, ZnSnO$_4$, Zn$_2$SnO$_3$), as a class of complex metal oxide was widely studied as a fire retardant [11, 12], lithium-ion battery material [13], catalysts owing to their environmentally-friendly, nontoxic, safe and high-effective flame and smoke-retardant properties, and lithium-ion storage properties [14]. However, the wide bandgap of ZnSn(OH)$_6$ is a big challenge to the absorption of visible light when

applying this material [6, 15, 16]. As a result, carbon quantum dots were coated on $ZnSn(OH)_6$ to improve the photon absorption, thus, enhancing the photocatalytic ability of the material. Besides, the photocatalytic membrane application has been considered a better strategy to achieve a better degradation result. To facilitate a better distribution of an active species of the catalyst into the degradation of dye pollutants, applying the photocatalytic membrane has been considered a better strategy to achieve a better result. The photocatalytic membrane has a high potential to degrade the organic pollutants by producing oxygen-reactive radicals under light irradiation. As a result, combining photocatalysts and membranes hold the potential to increase the material's photocatalytic applicability as well as its applicability in all fields. [17, 18].

This study used carbon quantum dots to improve the photocatalytic performances of $ZnSn(OH)_6$ for removing methylene blue (MB) from water. Firstly, the shapes of $ZnSn(OH)_6$ were controlled by adding different amounts of sodium hydroxide (NaOH). Then, the hydrothermal method was used for carrying out the carbon-doped on $ZnSn(OH)_6$ using other reaction times, temperatures, and different percentages of carbon-doped on the catalyst to control the photodegradation under visible light and coated on the membrane for improving the degradation of MB.

2. Experimental Section

2.1. Material and Chemical. All the chemicals were used without being treated. Tin (IV) Chloride Pentahydrate $SnCl_4 \cdot 5H_2O$ manufactured by Alfa aesar, Zinc Acetate Dehydrate $Zn(CH_3COO)_2 \cdot 2H_2O$ and glucose manufactured by Sigma, sodium hydroxide made in Japan, ethanol C_2H_5OH manufactured by Alfa aesar, double distilled water, MB manufactured by Alfa aesar, and Nitrogen and Oxygen manufactured by Mingyang special gas Co., purity 99.99%, respectively.

2.2. Preparation of Zinc Stannate. The preparation of the different shapes of zinc stannate followed the previous studies reported by Pham, Li, and coauthors [19, 20]. 0.7 g of pentahydrate tin tetrachloride and 0.44 g of zinc acetate dehydrate were added in two backers separately, dissolved in 5 mL of double distilled water, and stirred for 10 min. Different amounts of sodium hydroxide solution (4, 6, and 8 mL of 3 M) were added dropwise. After that, the solution was stirred for 10 min, then 10 mL of 40% aqueous ethanol solution was added and stirred again for 10 min. The solution was put into an autoclave at different temperatures (120, 140, and 160°C). Those temperatures have been chosen to avoid the deformation of the material because at around 120–150°C, a hydrated form of zinc stannates termed zinc hydroxy stannate ($ZnSn(OH)_6$) or ZHS occurs during hydrothermal development [21].

2.3. Preparation of Carbon-Doped Zinc Stannate. The preparation of the different shapes of carbon-doped zinc stannate followed the previous study reported by Li and coauthors [22]. The carbon-doped zinc stannate was

prepared by the different percentages of glucose (1, 5, and 10%) used for the carbon's source and mixed with a small amount of double-distilled water, then stirred for 10 min and doped into the solution of zinc stannate, and then mixed for 30 min. Afterward, follow the same process above of the hydrothermal method by using different temperatures.

2.4. Catalyst Coating Membrane. The catalyst coating membrane was applied by modifying the polyvinylidene fluoride (PVDF) membrane as shown in Figure 1(a), the low-temperature plasma system was operated as shown in Figure 1(b), and the operation parameter in Table 1. To prepare the membrane coating 0.20 g of catalyst was added in 5 mL of 20% ethanol solution, the mixture was stirred and mixed by ultrasonic vibration, and the membrane was manually immersed in the uniform mixed solution for 30 min until the catalyst was completely coated on both sides of the membrane. Afterward, the coated membrane was removed from the dish and exposed to air drying for one day at room temperature. Then, the membrane coated with the catalyst was adhered to the membrane surface of a 10×10 cm flat frame (Figure 1(c)) using the type of AB glue to join the membrane with the frame, and the inner dimensions of the reaction tank are detailed in Table 2.

2.5. Photocatalytic Characteristics. The surface morphology was determined by scanning electron microscopy (SEM, Model: ZEISS EVO MA 10, ZEISS EVO LS 10). The X-ray diffraction (XRD) pattern uses a Bruker D8-Advance 5005 with Cu Kα radiation ($\lambda = 0.1540$ nm) to determine the samples' phase composition and crystal structure. The function group and bonding in the catalyst were analyzed by Fourier transform infrared spectroscopy on an FT/IR-4700 FTIR Spectrometer from JASCO. The material's diffuse reflectance spectroscopy (DRS) was measured in a wavelength range of 200–800 nm using a UV-Vis spectrometer (JASCO-V550). The surface area analysis by Brunauer–Emmett–Teller (BET) and the pore structure by Barrett–Joyner–Halenda (BJH) were measured by the US ASAP 2020 nitrogen adsorption instrument.

2.6. Modified Photocatalytic Membrane Experiment. In this study, the photocatalytic membrane test as shown in Figure 2 was used with MB as the target pollutant by batch experiment. The investigation was carried out with the photocatalytic membrane degradation experiment with 100 mL of 20 ppm of MB for 12 h at room temperature, and the sample was analyzed every hour. The visible light source was a lamp of 110 V, and 12 W, and the photocatalytic activities were measured with the optimum wavelength ($\lambda = 665$ nm) by spectrophotometer GENESYS 10 UV.

3. Result and Discussion

3.1. Effect of Different NaOH Concentrations on the Shape of Zinc Stannate. The evolution of microscopic image has been shown differently by adding different amounts of NaOH (4,
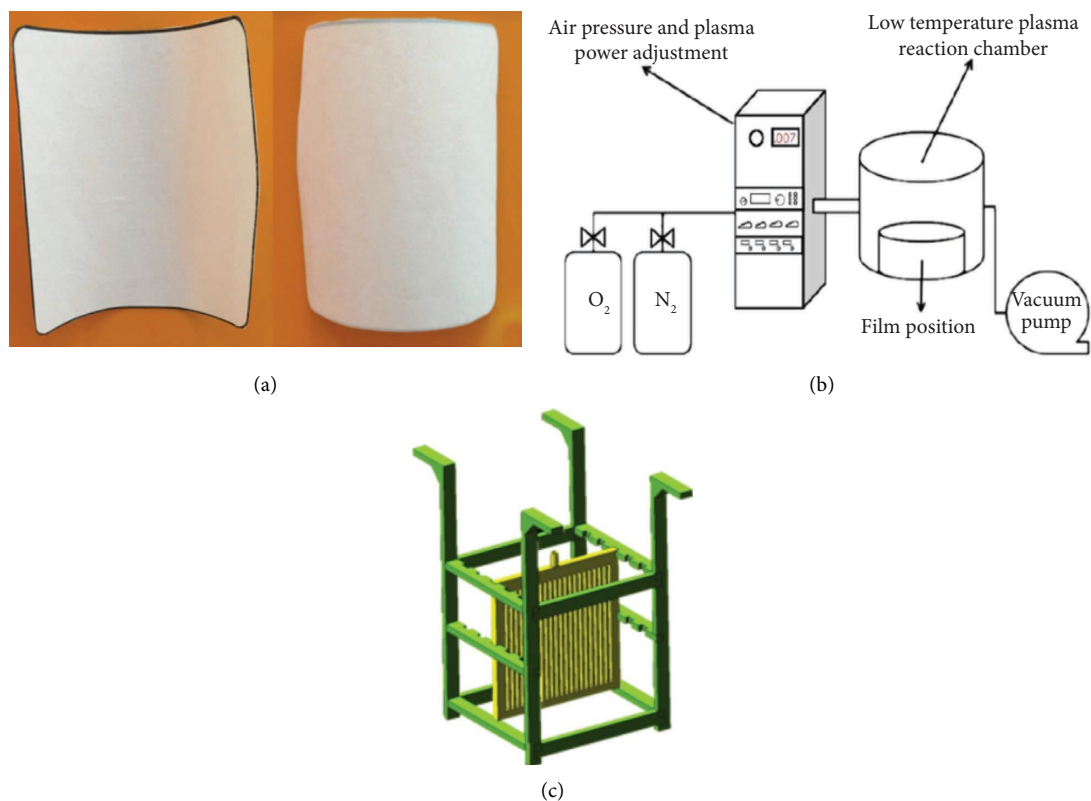
(a)

(b)

(c)

FIGURE 1: PVDF membrane (a). Schematic diagram of low-temperature plasma (b). Architecture of the film holder (c).

TABLE 1: Operating parameters of low-temperature plasma processing.

	Operating parameter
Power	100 W
Plasma processing time	120 sec
Reflectance	40%
Nitrogen	20 sccm
Oxygen	5 sccm
Temperature	60°C

TABLE 2: Design parameters of the film reaction tank.

|	Design parameters
Slot body—long	15 cm
Slot—width	15 cm
Slot—high	20.5 cm
Tank—volume	4.5 L
Film template—long	10 cm
Film template—wide	10 cm
Film template—thickness	0.6 cm
Film template—water outlet	0.3 cm
Film template—frame width	1 cm
Film template—permeable zone	0.3 cm ×20 pieces
Film holder—long	11 cm
Film holder—wide	11 cm
Film holder—high	16 cm
Film holder—template Jack	0.7 cm
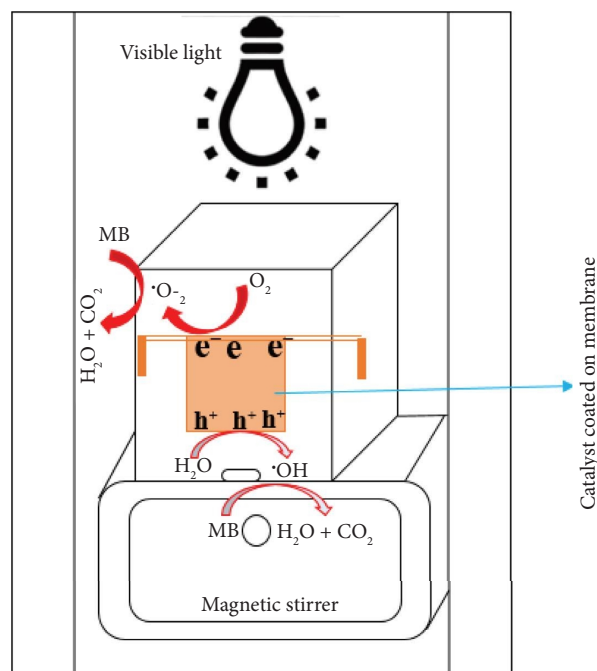
FIGURE 2: Schematic diagram of the photocatalytic film module.

6, and 8 mL of 3 mol·L^{-1}) in the preparation of the zinc stannate from cubic, truncated tetradecahedron, and octahedron, respectively (Figure 3). The direct relationship
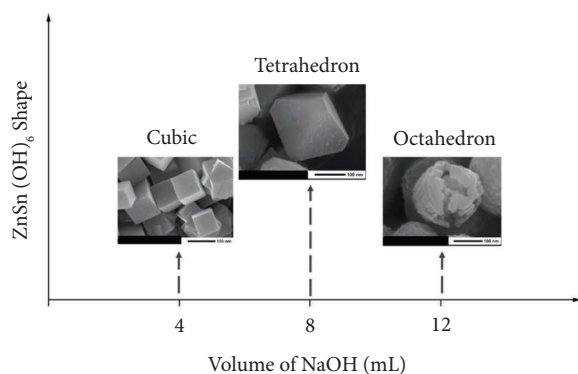
Figure 3: Relationship between the shape of zinc stannate and the content of sodium hydroxide.

between the NaOH concentration and the shape of the sample can be seen and better understood below in the scanning electron microscopy (SEM) analysis. As shown in Figure 3, the morphology of $ZnSn(OH)_6$ changes with different NaOH dosages. The results indicated that NaOH dosage is a primary factor affecting the hydrothermal synthesis process of $ZnSn(OH)_6$.

3.2. SEM Analysis of Different Reaction Times on the Shape of Zinc Stannate.
The direct relation between reaction time and the shape of the sample can be seen clearly in SEM results, as shown in Figure 4. The shape and structure of the octahedron (Figure 4(b) (A–C)) were not completely achieved when the preparation time was 2 h (Figure 4(b) (A)), and the zinc oxyhydroxide polyhedral structure began to collapse when the reaction time was 6 h (Figure 4(b) (C)), so the result showed that the optimum preparation time was 4 h (Figure 4(b) (B)). The shape of the truncated tetradecahedron (Figure 4(a) (A–C)) and the octahedron were formed simultaneously. In addition, the cubic (Figure 4(c) (A–C)) was presented when the preparation times were 2, 4, and 6 h. Therefore, 4 h was the optimal reaction time to simultaneously obtain the three shapes (cube, octahedron, and tetradecahedron).

3.3. Analysis of XRD of Different Morphology of Zinc Stannate.
The analysis of XRD results of zinc stannate hydroxide is shown in (Figure 5(a)). The 16 diffraction peaks of these three samples were 19.7, 22.8, 32.4, 36.4, 38.2, 40.0, 43.4, 46.5, 51.0, 52.4, 57.9, 61.7, 68.0, 71.5, 72.7, and 77.3°, respectively, with (111), (200) of $ZnSn(OH)_6$, (220), (013), (311), (222), (321), (400), (331), (420), (422), (511), (440), (135), and (531) compared with the database (JCPDS card No. 73–2384) and previous studies [23–25]. The crystal plane result indicates that $ZnSn(OH)_6$ composites have been successfully prepared, with no impurities.

For further comparison, it can be seen that the peak of the three different shapes of zinc stannate was expected to be different at the 22.8° (200) and 32.4° (220) crystal plane positions. The peaks (220) and (200) increased by increasing the amount of NaOH. It was due to sodium hydroxide's influence on the materials' preparation.

After confirming the effect of sodium hydroxide on the crystallites of zinc stannate, the relationship between the reaction time and the formation of the zinc stannate cube was established in Figure 5(b). The experiment was designed for 2, 4, 6, and 8 h as the operating parameters of the hydrothermal reaction time. XRD confirmed the modification of the crystal lattice, the crystal face of zinc stannate appeared in 6 h showing the most vigorous peak intensity of the tetrahedron. On the other hand, in samples 2 and 8 h, the crystallinity of the remaining samples is almost similar. The result showed that 6 and 4 h are the best preparation times, and further explanation also appeared in the SEM section.

The XRD analysis of zinc hydroxide with different amounts of carbon content is shown in Figure 5(c). The result shows the zinc hydroxide content of 1% of carbon and pure zinc hydroxide denoted a similar diffraction pattern and classified as the diffraction peaks of zinc stannate (JCPDS card No. 73-2384). Thus, 1% carbon-doped on the samples did not change the physical structure. However, the XRD analysis could not detect any diffraction peak spectrum by adding more than 10% of carbon to the samples; it could be explained that the excessive amount of carbon destroys the crystal structure of the zinc stannate and no longer exhibited the physical form of the material and might be limited for potential photodegradation of the pollutant.

The effect of temperature on the crystallinity of zinc stannate (Figure 5(d)) can be known from the primary peak intensity of the (200) crystal plane [6], the XRD peak intensity of the crystal face was 18,499, 19,283, and 25,979 nm at 120, 140, and 160°C, respectively, which means that the crystallinity of zinc stannate increased with increasing the temperature.

3.4. FTIR Analysis of Different Shapes of Zinc Stannate.
The FTIR absorption peak positions of the three different shapes of zinc stannate (Figure 6(a)), indicating that the functional groups of zinc stannate were not changed by adding NaOH solution. The broad peak of 3000–3500 cm^{-1} and the characteristic peaks around 1620 cm^{-1} are attributed to the surface water molecules of zinc stannate or the vibration of ^-OH bonds in crystal water [26]. The characteristic peak around 2341 cm^{-1} is attributed to CO_2 adsorbed on the catalyst surface [27, 28]. The peak around 1176 cm^{-1} is related to the vibration of the zinc stannate zinc Sn-OH bond, and the characteristic peaks of 540 cm^{-1} and 779 cm^{-1} are attributed to the internal structure of zinc stannate and O-vibration, respectively, [26, 29]. Those characterization peaks explain that the Sn-OH bond's vibration is responsible for producing OH radicals. In addition, superoxide was created by the reaction of O-vibration on the catalyst's surface with an electron. Thus, zinc stannate's surface-rich hydroxyl group structure and oxygen vibration were beneficial in producing hydroxyl radicals and superoxide with strong oxidizing ability during the photocatalytic reaction, which can effectively degrade the environmental organic pollutants under visible light. On the other hand, as reported by Jose and coauthors [30], the functional groups of the $ZnSn(OH)_6$ do not change at differences in synthesized temperature.
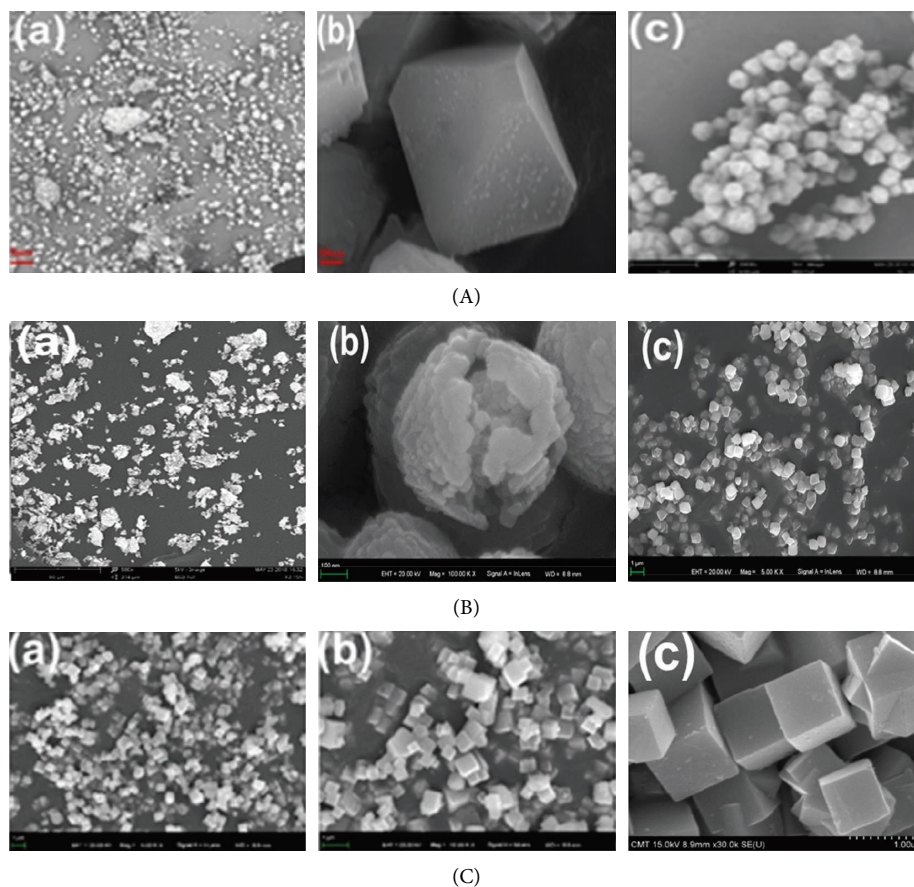
(A)

(B)

(C)

FIGURE 4: Tetrahedral zinc stannate (A), octahedral zinc stannate (B), and cubic zinc stannate (C) for 2 h (a), 4 h (b), and 6 h (c) preparation time.

Figure 6(b) illustrates how changing temperatures affect the functional group makeup of cube zinc stannate. The bottom of the zinc stannate was used as a control, and the position of absorption peaks was the same, which means that the temperature did not change the surface of the functional group of the composition of zinc stannate using 1% of carbon-doped in the sample by the regulation of hydrothermal method. In addition, the group still has a large amount of hydroxide on the surface that promotes the progress of the photocatalytic reaction.

3.5. Brunauer–Emmett–Teller (BET) and the Pore Structure Barrett–Joyner–Halenda (BJH) Analysis.

The surface structure of three shapes of zinc stannate was analyzed by the N_2 adsorption-desorption curve (Figures 7(a)–7(c)). The isotherms belong to the isotherm adsorption curve of class IV. Besides, according to the international union of pure and applied chemistry classification, three shapes of zinc stannate can be found, and the hysteresis belongs to the H3 type. The specific surface areas of cubes, octahedrons, and truncated tetradecahedrons were 8.7, 2.8, and 2.3 $m^2 \cdot g^{-1}$, respectively. Due to the large crystal size of the sample, the specific surface areas were relatively small.

The corresponding BJH pore size distribution is shown in Figure 7(d), and it is shown that the cubic zinc stannate was beneficial to form a structure with a larger pore size; the average pore size of cubic zinc stannate, octahedron zinc stannate, and truncated tetrahedron zinc stannate was 88, 61, and 26 nm, respectively. A larger surface area and porous structure increase the number of reactive sites on the catalyst's surface, which is beneficial for the adsorption of pollutants during the reaction process and enhances photocatalytic activities. So the cubic zinc stannate might be the best material in this study [15, 31, 32].

3.6. The UV-DRS Absorption Spectrum Analysis.

The UV-DRS absorption spectrum analysis was shown in Figure 8. The DRS absorption spectrum analysis was observed from Figure 8(a), the absorption peaks of octahedron zinc stannate, tetradecahedron zinc stannate, and cubic zinc stannate 275, 280, and 320 nm, respectively. The results clearly showed the light absorption range change by the shapes of zinc stannate. This analysis proved that the absorption peaks edge of cubic zinc stannate was closer to the visible light area, so the position of the light adsorption on the cube zinc stannate compared to other materials can be easily applied for the production of OH radicals and superoxide and can achieve the best photocatalytic activities under visible light. Besides, the indirect bandgap of the materials was shown in Figure 8(b), the bandgap of octahedron zinc stannate, tetradecahedron zinc stannate, and cubic zinc stannate are 2.93, 3.06, and 3.01 eV, respectively.
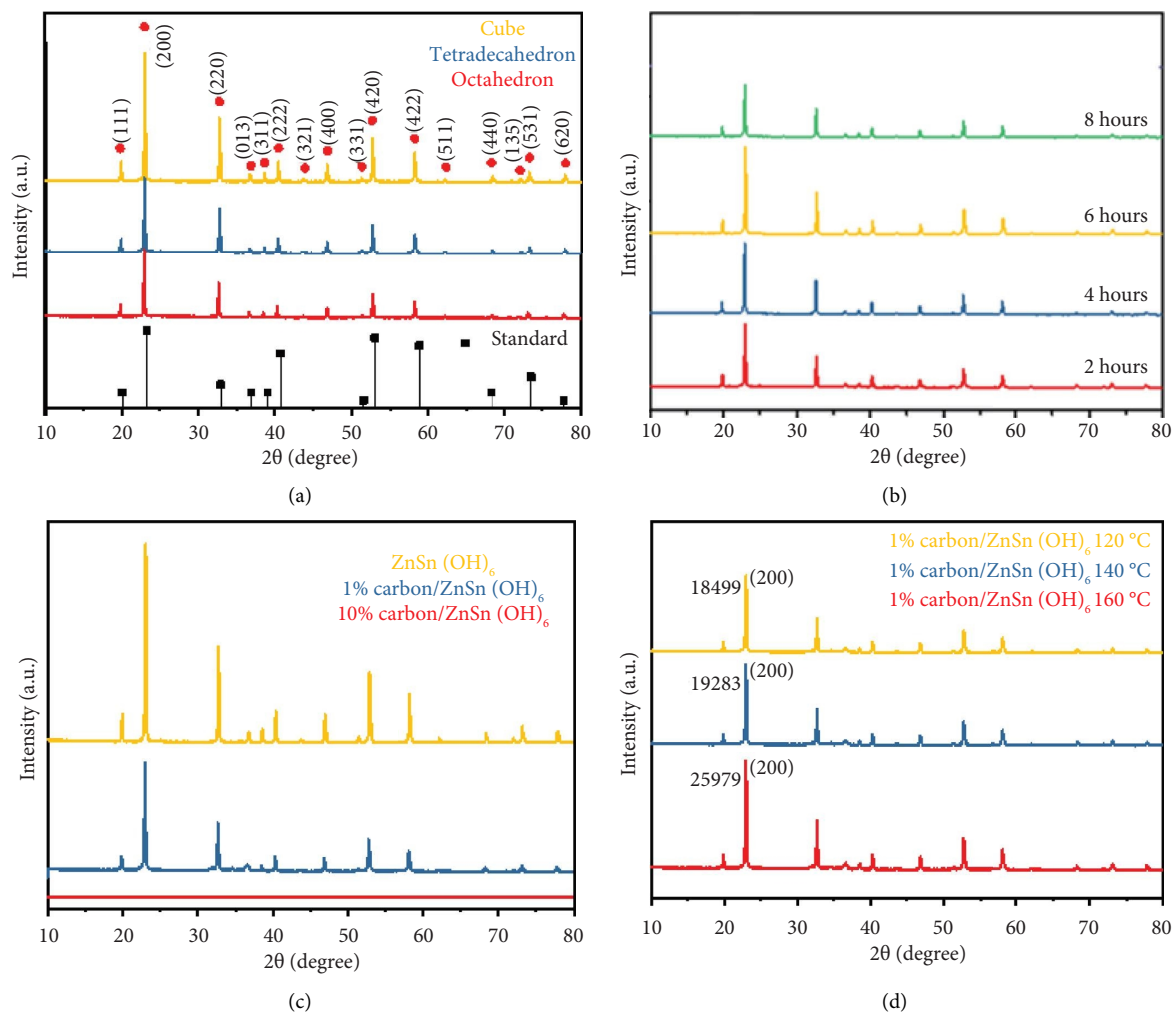
Figure 5: XRD comparison result of various shapes (a). Effect of different reaction times of zinc stannate cube (b). Comparison of XRD of cube zinc stannate before and after doping (c). Different synthetic temperature cubic zinc hydrate XRD (d).
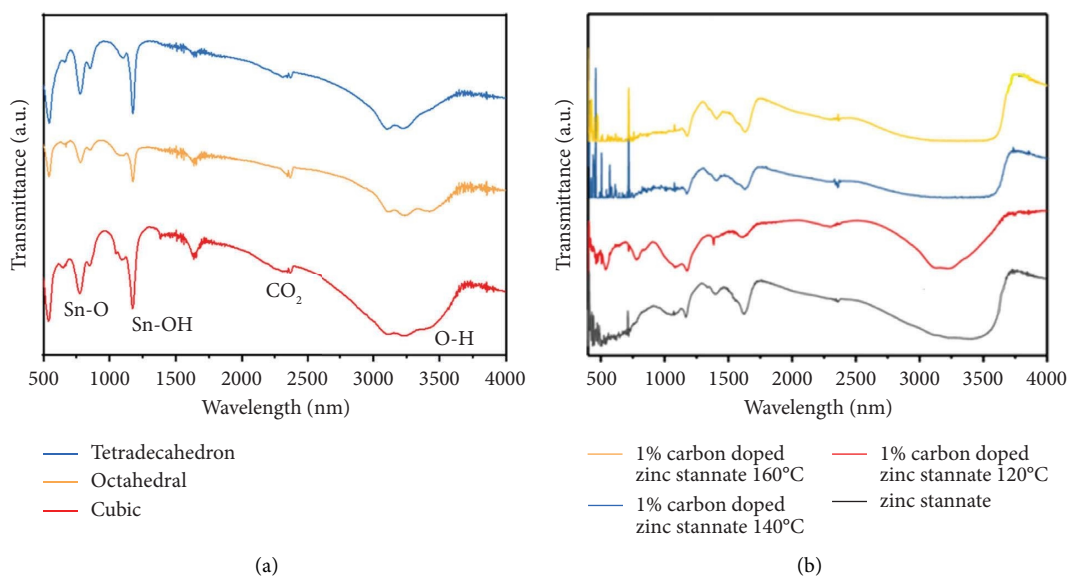

Figure 6: FTIR spectra of different shapes of zinc stannate (a). FTIR spectrum of cube zinc stannate at different temperatures (b).
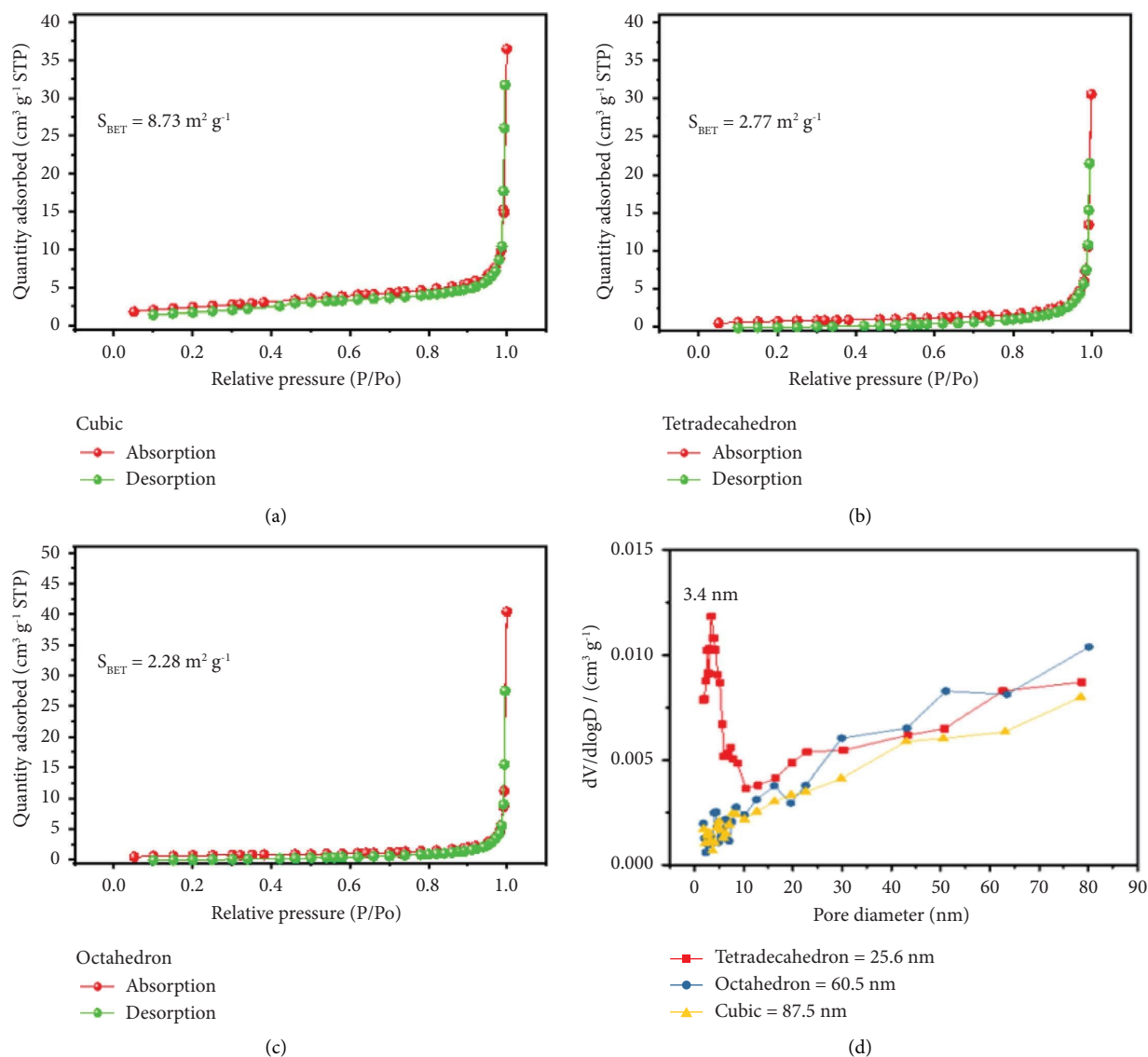
(a)

(b)

(c)

(d)

FIGURE 7: Specific surface areas of various shapes of zinc stannate (a, b, c). Pore size distributions of different shapes of zinc stannate (d).

These results indicated that the band structure of each shape is different, which directly affects the photocatalytic performance and mechanism of the materials. So the indirect bandgaps of different morphologies of $ZnSn(OH)_6$ are approximately 3.0 eV. Based on the previous study [33, 34], the conduction band (CB) and the valance band (VB) of the $ZnSn(OH)_6$ are approximately −0.52 and 3.16 eV vs. NHE, respectively.

3.7. Analysis of Photocatalytic Degradation Efficiency of Zinc Stannate with Different Carbon Doping Amounts. The photocatalytic efficiency of zinc stannate with different amounts of carbon on the samples was determined by the degradation of MB dye under visible light (Figure 9(a)). The MB degradation efficiency of various amounts of carbon dopes on cubic zinc stannate was ranked as follows. 0, 1, 5, and 10% carbon with degradation efficiency of 19.13, 89.74,

69.1, and 30.93%, respectively. It can be seen that the photocatalytic efficiency decreases by increasing the amount of carbon by more than 1%. It might explain that an excess amount of carbon reduced the photoreaction in the reactor by decreasing the light penetration and the photoactivity of zinc stannate. The results and the previous XRD analysis demonstrate that excessive carbon destroys stannic acid.

As mentioned in the previous section, because the pure zinc stannate cannot work in visible light, so 1% carbon-doped was used as a reference here. As can be seen in Figure 9(b) with different shapes of the samples, the degradation efficiency of zinc stannate for MB degradation was ranked as follows 89.74, 82.06, and 71.88% with the cube, truncated tetradecahedral, and octahedron, respectively. This result is consistent with the DRS analysis in that the light absorption wavelength range of the cubic zinc stannate is much closer to visible light compared to other shapes, and the results of BET and BJH showed a larger
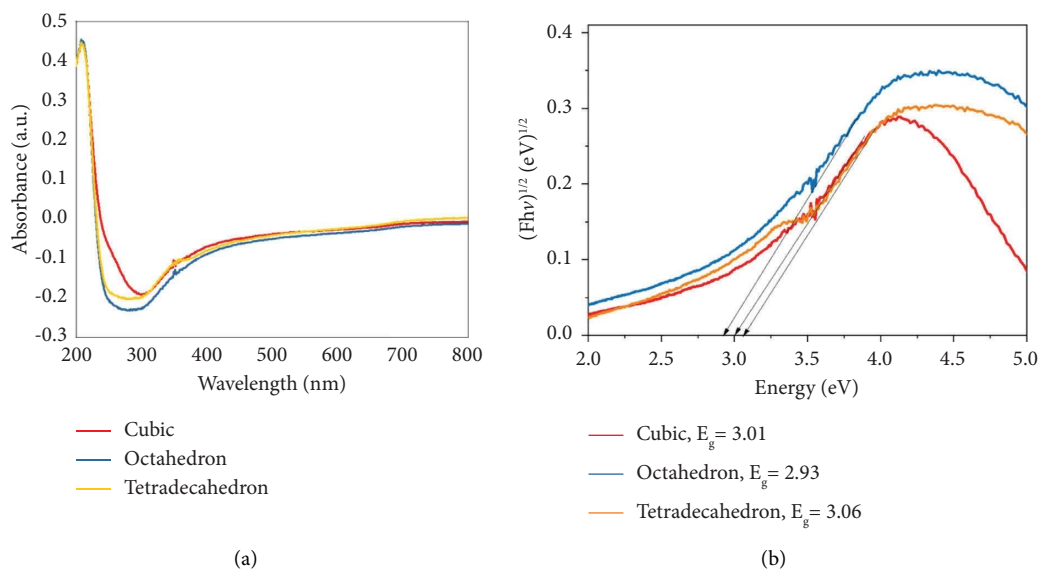
(a)

(b)

FIGURE 8: DRS absorbance spectra (a) and indirect bandgap of the materials (b).
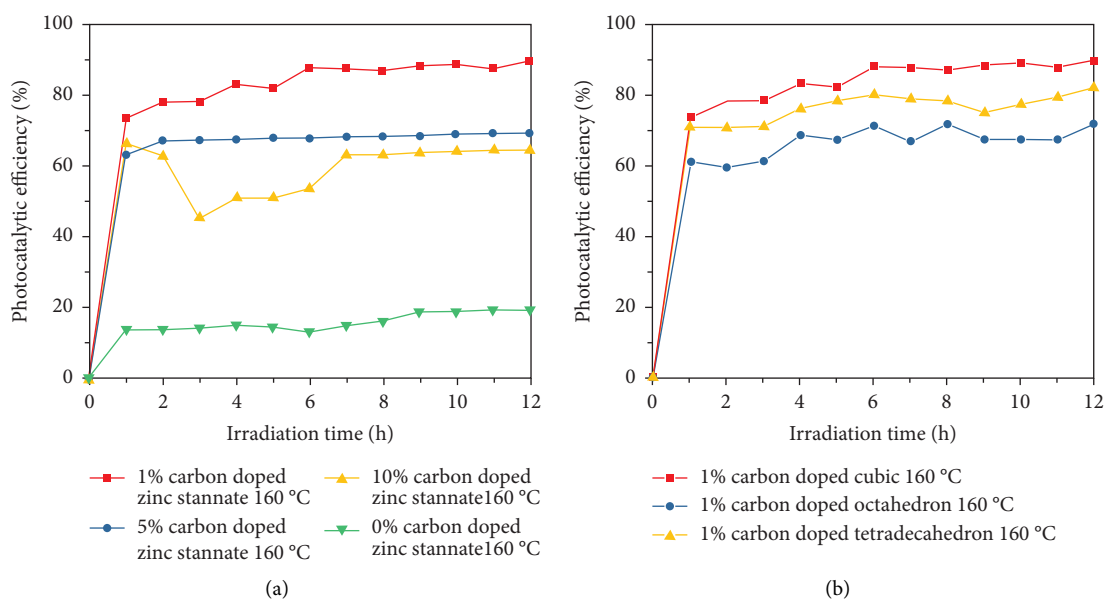

(a)

(b)

FIGURE 9: Comparison of methyl blue catalytic efficiency of cubic zinc stannate with different carbon doping ratios (a). Comparison of methyl blue catalysis efficiency of 1% carbon-doped zinc stannate in different shapes (b).

specific surface area and having a more significant number of mesopores, all enhancing the photocatalytic efficiency [35, 36].

3.8. Photocatalytic Efficiency Analysis of 1% Carbon-Doped Zinc Stannate at Different Reaction Temperatures. The degradation of MB dye under visible light determined the photocatalytic membrane efficiency of 1% carbon-doped on zinc stannate at different temperatures. In addition, cubic, octahedral, and tetradecahedral carbon blends were evaluated in the impurity content was 1%. The photocatalytic efficiency was optimum at 160°C (Figure 10(a)). The

photodegradation results were matched with the XRD analysis because the higher photocatalytic efficiency is denoted at the higher crystallinity simultaneously. So, the material's crystallinity positively correlates with the photocatalytic efficiency. The results may be explained that a complete decomposition of glucose into carbon doping on the zinc stannate crystal was better by increasing the temperature; the cube's shape and 1% of carbon-doped on zinc stannate showed the best performance for photocatalytic efficiency evaluations, with 89.74% of degradation of MB under visible light irradiation. Figures 10(b) and 10(c) show the degradation efficiency of various synthetic temperatures of octahedron and tetradecahedron. Both of them at 1% of
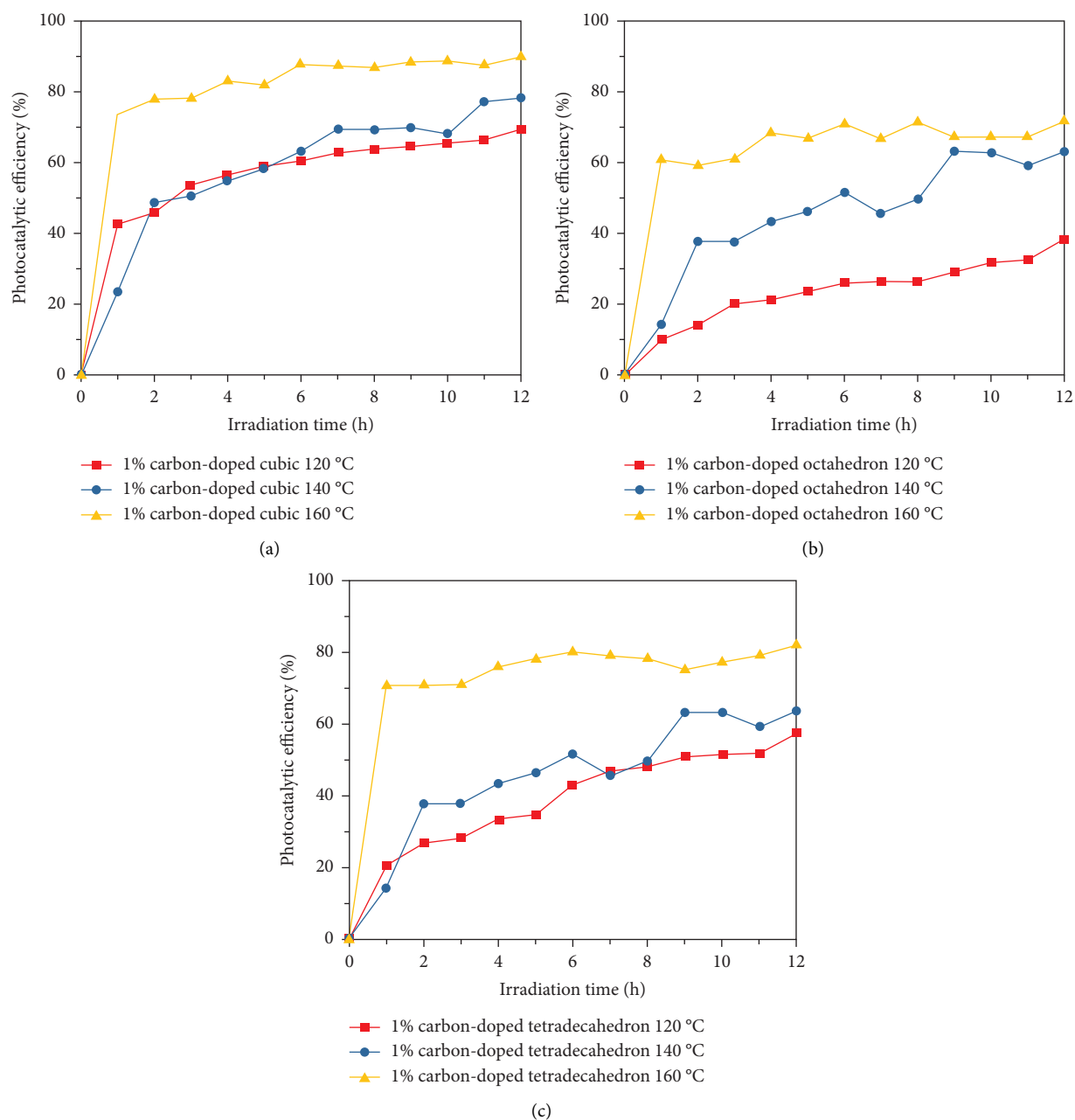
FIGURE 10: Degradation efficiency of 1% carbon-doped cubic zinc stannate sulfate at different temperatures (a), degradation efficiency of 1% carbon-doped octahedron zinc stannate sulfate at different temperatures (b), and degradation efficiency of 1% carbon-doped tetradecahedron (c).

carbon-doped on zinc stannate and tetrahedral shape denoted that the photocatalytic efficiency was increased with increasing the temperature. Furthermore, the cube-shaped 1% carbon-doped on tin hydroxide zinc acid exhibited the best performance in all photocatalytic efficiency evaluated. The removal efficiency of MB under visible light irradiation was reached at 89.74% and was effectively consistent with the characterizations above.

The result was also compared in Table 3 to some previous studies on the degradation of dyes based on $ZnSn(OH)_6$ photocatalyst and realized that most of that experiments used high energy (UV-light) and low dyes concentration to

induce the degradation of dye using $ZnSn(OH)_6$. Our research showed a better performance due to the highly efficient degradation of high-concentration dyes under visible light. Although the efficiency of the catalyst interval is high, applying the photocatalytic membrane can be considered a better strategy of innovation to achieve a better degradation result.

3.9. Photocatalytic Mechanism of Degradation of MB. The photocatalytic mechanism of the proposed carbon-doped zinc stannate for MB degradation under visible light is

TABLE 3: Comparison table of dye degradation over catalyst based on $ZnSn(OH)_6$.

| Catalyst	Pollutants	Concentration (ppm)	Light source	Removal (%)	References
g@AgCl/ZnSn(OH)$_6$	Rhodamine B	10	Visible light	99.86	[37]
g@AgCl/ZnSn(OH)$_6$	Crystal violet	10	Visible light	98.56	[37]
C-ZnSn(OH)$_6$	Methylene blue	10	UV-light	98	[38]
S-ZnSn(OH)$_6$	Rhodamine B	10	Visible light	100	[24]
ZnSn(OH)$_6$	Methylene blue	10	UV-light	100	[15]
C-ZnSn(OH)$_6$	Methylene blue	20	UV-light	95	[23]
C-ZnSn(OH)$_6$ coated membrane	Methylene blue	20	Visible light	89.74	This study
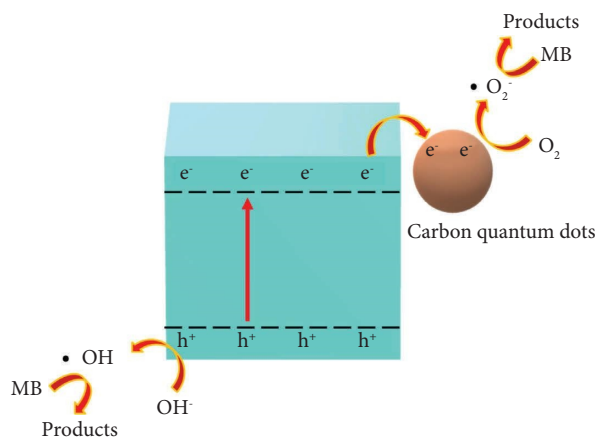
FIGURE 11: Photocatalytic mechanism of the proposed carbon-doped zinc stannate for MB degradation under visible light.

shown in Figure 11. The electrons were excited and moved to the CB of $ZnSn(OH)_6$ to generate excess e^- and h^+ under visible light. Under the support of carbon quantum dots, the excess e^- in the CB of $ZnSn(OH)_6$ could transfer to the carbon dots for the reaction reactions. According to the discussed band structure, the CB of the $ZnSn(OH)_6$ (-0.52 eV vs NHE) is higher than the $O_2/(\bullet O_2^-)$ (-0.33 eV vs NHE), so the excess e^- can reduce O_2 to form $(\bullet O_2^-)$ radicals. The $(\bullet O_2^-)$ radicals prompted the oxidization of MB. On the other hand, the excess h^+ produced $\bullet OH^-$ radicals from water. Then, the $\bullet OH^-$ radicals degraded MB [22, 25]. The recombination of e^- and h^+ was reduced under supporting carbon quantum dots, which helped enhance the photocatalytic performances of the material. After coating the carbon-doped zinc stannate on the membrane, by turning on the light, the electrons (e^-) were moved to the conduction band (CB), and the holes (h^+) were active in the valance band (VB) as shown in equation (1). Equation (2) shows the production of the superoxide ($\bullet O_2^-$), when the electrons were reacted with the oxygen on the surface of the catalyst coated on the membrane. Then, equation (3) explains the production of the OH radicals ($HO\bullet$). Finally, the degradation products are shown in equations (4) and (5).

$$C@ZnSn(OH)_6 + h\nu \longrightarrow C@ZnSn(OH)_6 \left(h^+VB + e^-\, CB\right), \quad (1)$$

$$O_2 + e\overline{CB} \longrightarrow \bullet O_2^-, \quad (2)$$

$$H_2O + h^+ \longrightarrow HO\bullet + H^+, \quad (3)$$

$$MB + \bullet O_2^- \longrightarrow \text{Degradation products}, \quad (4)$$

$$MB + \bullet OH \longrightarrow \text{Degradation products}. \quad (5)$$
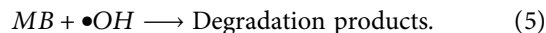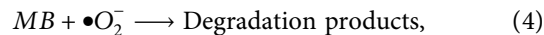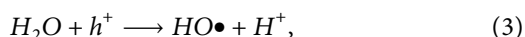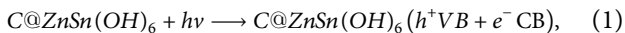
4. Conclusions

The result of the experiment confirmed that the preparation of carbon-doped zinc stannate was effectively prepared by the hydrothermal method. The morphology of zinc stannate changed by adding different NaOH dosages. The effect of NaOH dosage and synthesis time on the morphology, specific surface area, and light absorption of ZnSn(OH) SEM, BET confirmed $_6$, and DRS. The BJH analysis showed that the cubic stannate composite had the best pore size. As a result, the BET showed the surface area of cubic zinc stannate ($8.7 \, \text{m}^2 \cdot \text{g}^{-1}$) to be better than tetradecahedron ($2.8 \, \text{m}^2 \cdot \text{g}^{-1}$) and octahedron ($2.3 \, \text{m}^2 \cdot \text{g}^{-1}$). In addition, the XRD and FTIR confirm no change in the crystal structure and chemical bonding between each shape of $ZnSn(OH)_6$. The results show that 1% of carbon-doped on $ZnSn(OH)_6$ cubic by hydrothermal method at 160°C for 6 h reached the highest photocatalytic efficiency of MB (89.74%) under visible light. The photocatalytic results confirmed that the cubic shape of $ZnSn(OH)_6$ is a potential catalyst for the photodegradation of MB, and carbon-$ZnSn(OH)_6$ coupled with a photocatalytic membrane is promising for future applications.

Data Availability

The data used to support the study are available from the corresponding author upon request.

Conflicts of Interest

The authors declare there are no conflicts of interest.

Acknowledgments

References

[1] A. C. Ni'am, E. Fenelon, E. Ningsih, Y. W. Mirzayanti, and E. Kristanti, "High efficiency adsorption of hexavalent chromium from aqueous solution by *Samanea saman*

activated carbon," *Adsorption Science and Technology*, vol. 2022, Article ID 8960379, 10 pages, 2022.

[2] E. Fenelon, A. C. Ni'am, Y. F. Wang, and S. J. You, "Study of the potential of La/Bi$_2$S$_3$ catalyst for photodegradation of acid yellow 42 dye under visible light," *Journal of Nanomaterials*, vol. 2022, Article ID 2990466, 13 pages, 2022.

[3] E. Fenelon, D. P. Bui, H. H. Tran et al., "Straightforward synthesis of SnO2/Bi2S3/BiOCl–Bi24O31Cl10 composites for drastically enhancing rhodamine B photocatalytic degradation under visible light," *ACS Omega*, vol. 5, no. 32, Article ID 20438, 20449 pages, 2020.

[4] S. Phanichphant, A. Nakaruk, K. Chansaenpak, and D. Channei, "Evaluating the photocatalytic efficiency of the BiVO4/rGO photocatalyst," *Scientific Reports*, vol. 9, no. 1, Article ID 16091, 2019.

[5] Y. Lin, J. Ma, W. Liu, Z. Li, and K. He, "Efficient removal of dyes from dyeing wastewater by powder activated charcoal/titanate nanotube nanocomposites: adsorption and photoregeneration," *Environmental Science & Pollution Research*, vol. 26, no. 10, Article ID 10263, 10273 pages, 2019.

[6] M.-T. Pham, D.-P. Bui, I.-F. Lin et al., "Enhanced near-visible-light photocatalytic removal of formaldehyde over Au-assisted ZnSn(OH)6 microcubes," *Environmental Technology & Innovation*, vol. 20, Article ID 101112, 2020.

[7] X. Li, J. Natsuki, and T. Natsuki, "A recyclable silver nanoparticles/graphene oxide nanoscroll composite photocatalyst," *Environmental Technology & Innovation*, vol. 21, Article ID 101210, 2021.

[8] E. Fenelon, A. Hussain, T.-H. Yang et al., "High photocatalyst module on degradation of extracted gas from soil under visible light," *Aerosol and Air Quality Research*, vol. 9, no. 12, pp. 2865–2878, 2019.

[9] E. Fenelon, S.-J. You, and Y.-F. Wang, "Photodegradation of nitrogen oxide under solar light using a facile synthesis catalyst," *Aerosol and Air Quality Research*, vol. 21, no. 10, Article ID 210128, 2021.

[10] H. Wang, X. Liu, P. Niu, S. Wang, J. Shi, and L. Li, "Porous two-dimensional materials for photocatalytic and electrocatalytic applications," *Matter*, vol. 2, no. 6, pp. 1377–1413, 2020.

[11] L. Yang, Y. Hu, F. You, and Z. Chen, "A novel method to prepare zinc hydroxystannate-coated inorganic fillers and its effect on the fire properties of PVC cable materials," *Polymer Engineering & Science*, vol. 47, no. 7, pp. 1163–1169, 2007.

[12] X. Zhang, X. Guo, S. Yang et al., "Double-network hydrogel with high mechanical strength prepared from two biocompatible polymers," *Journal of Applied Polymer Science*, vol. 112, no. 5, pp. 3063–3070, 2009.

[13] F. Han, W. C. Li, C. Lei, B. He, K. Oshida, and A. H. Lu, "Selective Formation of carbon-coated, metastable amorphous ZnSnO$_3$ Nanocubes containing mesopores for use as high-capacity lithium-ion battery," *Small*, vol. 10, no. 13, pp. 2637–2644, 2014.

[14] S. Roy, B. Banerjee, A. Bhaumik, and S. M. Islam, "CO2 fixation at atmospheric pressure: porous ZnSnO3 nanocrystals as a highly efficient catalyst for the synthesis of cyclic carbonates," *RSC Advances*, vol. 6, no. 37, Article ID 31153, 31160 pages, 2016.

[15] Z. Ren, D. Zhou, L. Zhang et al., "ZnSn(OH)6 photocatalyst for methylene blue degradation: electrolyte-dependent morphology and performance," *ChemistrySelect*, vol. 3, no. 39, Article ID 10849, 10856 pages, 2018.

[16] B. Zhai, H. Li, G. Gao et al., "A crystalline carbon nitride based near-infrared active photocatalyst," *Advanced Functional Materials*, vol. 32, no. 47, Article ID 2207375, 2022.

[17] T. E. Berger, C. Regmi, A. I. Schäfer, and B. S. Richards, "Photocatalytic degradation of organic dye via atomic layer deposited TiO2 on ceramic membranes in single-passflow-through operation," *Journal of Membrane Science*, vol. 604, Article ID 118015, 2020.

[18] A. Yadav, P. Sharma, A. B. Panda, and V. K. Shahi, "Photocatalytic TiO2 incorporated PVDF-co-HFP UV-cleaning mixed matrix membranes for effective removal of dyes from synthetic wastewater system via membrane distillation," *Journal of Environmental Chemical Engineering*, vol. 9, no. 5, Article ID 105904, 2021.

[19] Y. Li, B. Chen, P. Ouyang, Y. Duan, W.-J. Ong, and F. Dong, "Engineering ZnSn(OH)6 with ternary active sites-directed hydroxyl vacancies for robust deep C6H6 photo-oxidation: experiment and DFT calculations," *Chemical Engineering Journal*, vol. 451, Article ID 138695, 2023.

[20] M.-T. Pham, H.-H. Tran, T.-M. T. Nguyen et al., "Revealing DeNOx and DeVOC reactions via the study of the surface and bandstructure of ZnSn(OH)6 photocatalysts," *Acta Materialia*, vol. 215, Article ID 117068, 2021.

[21] S. Baruah and J. Dutta, "Zinc stannate nanostructures: hydrothermal synthesis," *Science and Technology of Advanced Materials*, vol. 12, no. 1, Article ID 013004, 2011.

[22] H. Li, W. Hong, Y. Cui, Q. Jia, and S. Fan, "High photocatalytic activity of C-ZnSn(OH)6 catalysts prepared by hydrothermal method," *Journal of Molecular Catalysis A: Chemical*, vol. 378, pp. 164–173, 2013.

[23] D. Li, P. Yan, Q. Zhao et al., "The hydrothermal synthesis of ZnSn(OH)6 and Zn2SnO4 and their photocatalytic performances," *CrystEngComm*, vol. 22, no. 29, pp. 4923–4932, 2020.

[24] X. Lian, Z. Chen, X. Yu et al., "Enhancing the photocatalytic activity of ZnSn(OH)6 achieved by gradual sulfur doping tactics," *Nanoscale*, vol. 11, no. 19, pp. 9444–9456, 2019.

[25] Y. Zhang, L. Wang, M. Yang, J. Wang, and J. Shi, "Carbon quantum dots sensitized ZnSn(OH)6 for visible light-driven photocatalytic water purification," *Applied Surface Science*, vol. 466, pp. 515–524, 2019.

[26] Q. He, J. Zi, B. Huang et al., "Controlled growth and thermal decomposition of well-dispersed and uniform ZnSn(OH)6 submicrocubes," *Journal of Alloys and Compounds*, vol. 607, pp. 193–197, 2014.

[27] E. P. Barannik, A. A. Shiryaev, and T. Hainschwang, "Shift of CO2-I absorption bands in diamond: a pressure or compositional effect? A FTIR mapping study," *Diamond and Related Materials*, vol. 113, Article ID 108280, 2021.

[28] Z. Hao, H. A. Bechtel, T. Kneafsey, B. Gilbert, and P. S. Nico, "Cross-scale molecular analysis of chemical heterogeneity in shale rocks," *Scientific Reports*, vol. 8, no. 1, p. 2552, 2018.

[29] T.-T. Gao, Z.-W. Li, L.-G. Yu, and Z.-J. Zhang, "Preparation of zinc hydroxystannate nanocomposites coated by organophosphorus and investigation of their effect on mechanical properties and flame retardancy of poly(vinyl chloride)," *RSC Advances*, vol. 5, no. 120, Article ID 99291, 99298 pages, 2015.

[30] M. Jose, G. Nithya, R. Robert, and S. A. M. B. Dhas, "Formation and optical characterization of unique zinc hydroxy stannate nanostructures by a simple hydrothermal method," *Journal of Materials Science: Materials in Electronics*, vol. 29, no. 4, pp. 2628–2637, 2018.

[31] H. Cheng, J. Wang, Y. Zhao, and X. Han, "Effect of phase composition, morphology, and specific surface area on the

photocatalytic activity of TiO2 nanomaterials," *RSC Advances*, vol. 4, no. 87, Article ID 47031, 47038 pages, 2014.

[32] T. Xu, X. Liu, S. Wang, and L. Li, "Ferroelectric oxide nanocomposites with trimodal pore structure for high photocatalytic performance," *Nano-Micro Letters*, vol. 11, no. 1, p. 37, 2019.

[33] X. Peng, M. Jiang, X. Wang et al., "Photocatalytic purification of contaminated air in intensive care units by ZnSn(OH)6 nanoparticles," *Environmental Science and Pollution Research*, vol. 28, no. 24, Article ID 31770, 31777 pages, 2021.

[34] C. Zhang, D. He, S. Fu et al., "Silver iodide decorated ZnSn(OH)6 hollow cube: room-temperature preparation and application for highly efficient photocatalytic oxytetracycline degradation," *Chemical Engineering Journal*, vol. 421, Article ID 129810, 2021.

[35] F. Amano, K. Nogami, M. Tanaka, and B. Ohtani, "Correlation between surface area and photocatalytic activity for acetaldehyde decomposition over bismuth tungstate particles with a hierarchical structure," *Langmuir*, vol. 26, no. 10, pp. 7174–7180, 2010.

[36] Z. Jiang, L. Feng, and J. Zhu, "RETRACTED: synthesis of magnetically recyclable porous CoFe2O4/Rh composites with large BET surface area for enhanced photocatalytic degradation of organic pollutant," *Ceramics International*, vol. 47, no. 13, pp. 18140–18149, 2021.

[37] F. Chen, Q. Yang, C. Niu, X. Li, C. Zhang, and G. Zeng, "Plasmonic photocatalyst Ag@AgCl/ZnSn(OH) 6 : synthesis, characterization and enhanced visible-light photocatalytic activity in the decomposition of dyes and phenol," *RSC Advances*, vol. 5, no. 78, Article ID 63152, 63164 pages, 2015.

[38] H. Lu, J. Lei, X. Li et al., "Synthesis and characterization of carbon-doped ZnSn(OH)6 with enhanced photoactivity by hydrothermal method," *Crystal Research and Technology*, vol. 51, no. 1, pp. 11–15, 2016.